



GEOLOGY

Incipient carbonate melting drives metal and sulfur mobilization in the mantle

Isra S. Ezad^{1*}, Martin Saunders², Svyatoslav S. Shcheka¹, Marco L. Fiorentini³,
Lauren R. Gorjovsky⁴, Michael W. Förster⁵, Stephen F. Foley^{1,5}

We present results from high-pressure, high-temperature experiments that generate incipient carbonate melts at mantle conditions (~90 kilometers depth and temperatures between 750° and 1050°C). We show that these primitive carbonate melts can sequester sulfur in its oxidized form of sulfate, as well as base and precious metals from mantle lithologies of peridotite and pyroxenite. It is proposed that these carbonate sulfur-rich melts may be more widespread than previously thought and that they may play a first-order role in the metallogenic enhancement of localized lithospheric domains. They act as effective agents to dissolve, redistribute, and concentrate metals within discrete domains of the mantle and into shallower regions within Earth, where dynamic physicochemical processes can lead to ore genesis at various crustal depths.

INTRODUCTION

The mobilization and anomalous concentration of chalcophile and siderophile elements into discrete mantle domains has been intimately linked to the behavior and mobility of sulfur (S), which is known to complex with base and precious metals into a variety of compounds (1–3). Much attention has therefore been directed toward understanding the solubility, saturation, and speciation of sulfur, as well as the partitioning behavior of chalcophile and siderophile elements into primitive melts (4–7). Specifically, most work has concentrated on basaltic compositions, which represent relatively high degrees of partial melting (12 to 15%) of their mantle source (8), whereas the behavior of sulfur and metals in the presence of incipient melts (<5% partial melting) is still very much poorly known. These incipient melts may, however, persist over a temperature range up to 300°C before major melting of silicates occurs (9).

The S solubility in silicate melts is strongly controlled by fO_2 (oxygen fugacity): Under reduced conditions, sulfur is present as sulfide, whereas sulfate is the soluble species under oxidized conditions (8). The transition of sulfide to sulfate also varies in fO_2 space as a function of melt composition, pressure, and temperature, as experimentally determined for silicate melts at pressures between 0.5 and 1.0 GPa (4, 10). In addition, the solubility of sulfur increases by an order of magnitude in silicate melts under oxidized conditions when stable as sulfate (11). Therefore, melts that are oxidized above the sulfide-sulfate transition at $\sim\Delta FMQ+1$ (Fayalite-Magnetite-Quartz) should incorporate higher concentrations of sulfur. Furthermore, in the absence of sulfide, chalcophile and siderophile elements (5, 12) will partition preferentially into silicate melts as their compatibility into coexisting oxides [e.g., chromite, ilmenite, and magnetite (13)], silicates (14), and alloys (15) may only occur at substantially more reducing conditions. Primitive oxidized melts (16, 17) are therefore expected to be

effective agents to dissolve, redistribute, and concentrate sulfur as well as chalcophile metals within the mantle and from the mantle to shallower regions within Earth (12, 18, 19).

Incipient melts may be locally generated in the mantle due to a substantial reduction in the solidus temperature associated with the presence of small amounts of volatile components such as H₂O and CO₂ (20–26). The composition of incipient melts generated from partial melting of volatile-bearing peridotite (1, 12) is carbonate-rich as long as conditions are sufficiently oxidizing ($>IW + 3$), which are expected at depths of 200 km or less in the mantle (27). The carbonate-rich incipient melts gradually change their composition with increasing degrees of partial melting ranging from carbonatite melts with typically <10 wt % SiO₂ and >40 wt % CO₂, to carbonate silicate melts with >25 wt % SiO₂ and <25 wt % CO₂ [e.g., (20, 28)]. We use the term carbonate melts hereafter to encompass this full geochemical diversity of carbonatite-like incipient melts, which are thought to be responsible for widespread metasomatism within the subcontinental lithospheric mantle (SCLM) [e.g., (19, 24, 29, 30)].

Mantle xenoliths, which sample the SCLM, commonly show evidence of carbonate metasomatism and may contain sulfides associated with carbonate minerals, suggesting a common association between S and carbon (C) (18, 23, 28–30). Despite the numerous experimental studies on the behavior S in silicate melts, relatively few experiments have explored the behavior of S in carbonate systems (5, 31). Nonetheless, these experiments demonstrate that sulfur solubility in carbonate melts also appears to be controlled by fO_2 and Fe content, akin to silicate systems (31).

Incipient carbonate melts are unlikely to ever reach the surface unmodified. Because of their high reactivity (12, 24), they may be responsible for the (re-)enrichment of the SCLM (31) in CO₂, H₂O, and Fe, and the enrichment of the lower crust in chalcophile and siderophile elements, such as sulfur (S), nickel (Ni), copper (Cu), and the platinum group elements (PGEs) (12, 29). The role of oxidized incipient carbonate melts in mobilizing sulfur, chalcophile, and siderophile elements from the mantle has not been experimentally investigated despite growing evidence from natural samples that conditions to liberate and concentrate S are favored during the earliest stages of mantle melting (12, 29, 32). Here, we present high-pressure, high-temperature experiments in combination with high-precision nanoscale analyses to demonstrate that carbonate melts are effective transport agents for

¹School of Natural Sciences, Macquarie University, North Ryde, Sydney, NSW 2109, Australia. ²Centre for Microscopy, Characterisation, and Analysis, University of Western Australia, Perth, WA 6009, Australia. ³Centre for Exploration Targeting, School of Earth Sciences, ARC Centre of Excellence for Core to Crust Fluid System, University of Western Australia, Perth, WA 6009, Australia. ⁴Department of Earth Sciences, University of Oxford, South Parks Road, Oxford OX1 3AN, UK. ⁵Research School of Earth Sciences, Australian National University, Canberra, ACT 2601, Australia.

*Corresponding author. Email: isra.ezad@mq.edu.au

S, as well as base and precious metals during the initial stages of mantle melting.

RESULTS

High-pressure experiments

Near-solidus melting experiments were conducted on two natural mantle compositions: a mica pyroxenite from western Uganda and a fertile spinel lherzolite from Lake Nyos, Cameroon. Both compositions were doped with small amounts of H₂O (1.5 and 1 wt %), CO₂ (3 and 2.5 wt %), S (0.8 and 0.5 wt %), and PGEs [800 and 500 parts per million (ppm) (weight)], respectively (full experimental details in Materials and Methods). The starting materials were loaded into Pt-lined double-chambered graphite capsules. The double-chambered capsules allowed for both compositions to be run simultaneously in the same experiment ensuring that both compositions were subject to the same pressure and temperature conditions. All experiments were conducted in a rapid quenching piston cylinder (33), to achieve temperatures between 750° and 1050°C and pressures of 2.5 GPa.

Incipient carbonate melts coexist with olivine (Olv), orthopyroxene (Opx), clinopyroxene (Cpx), spinel (Sp), and clinohumite (Ch) within the peridotite, and phlogopite (Phl), calcium titanite (Cattitanite), Cpx, and Olv within the pyroxenite. The stable carbonate phase for both rock compositions at subsolidus and near-solidus

conditions at 2.5 GPa is dolomite, and no melts were found in experiments at 750°C. The incipient melts for both compositions are carbonatites (1.91 to 2.30 wt % SiO₂, 32.33 to 42.61 wt % CaO; Supplementary Materials), which occur as poorly quenched glasses segregated toward one end of the experimental capsule (Figs. 1 and 2), as is typical for these low-viscosity highly mobile melts (20, 22, 34, 35).

Coexistence of sulfide and carbonate melts

Carbonate melts and sulfide blebs are concentrated along grain boundaries between silicate phases: While the sulfide blebs are easily visible in scanning electron microscopy (SEM) micrographs, the coexisting carbonate melts are not always visible (Fig. 3, B and D). To carry out cross-sectional imaging of the experimental samples and identify carbonate melts present along grain boundaries, transmission electron microscopy (TEM) imaging and TEM–energy dispersive spectroscopy (EDS) analysis were conducted.

The TEM images of the peridotite sample reveal the presence of ~1- μ m sulfide blebs surrounded by a matrix of clinohumite, with a thin veneer of quenched carbonate melt at the interface between sulfide and clinohumite (Fig. 3, A and B). High concentrations of Ca were found in thin coatings surrounding the sulfide blebs by TEM-EDS analysis (Fig. 3, B and D). The calcium cannot be attributed to the surrounding silicate minerals as the sulfide bleb within the

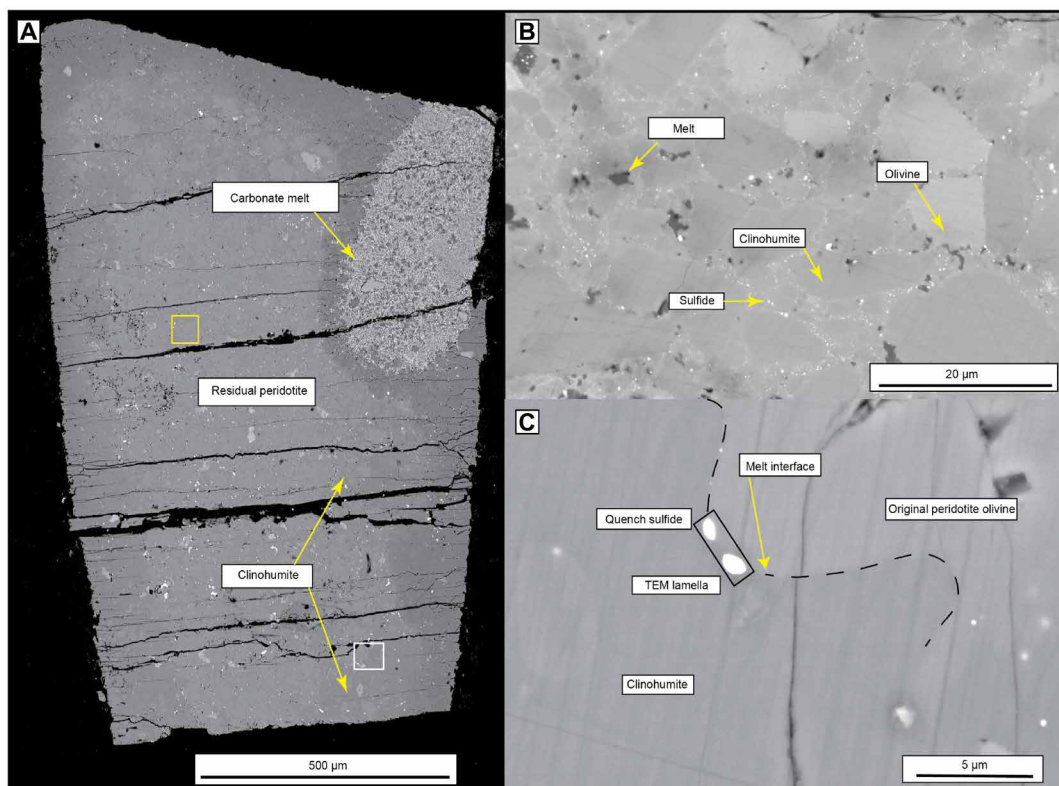


Fig. 1. Back-scattered electron micrographs of experimental sample M21-107 (2.5 GPa, 1050°C—peridotite) at different magnifications. (A) Overview of experimental charge. The carbonate melt is pooled at the top right and displays typical quench structure with sub-micrometer scale quench crystals in a fine-grained network. A clinohumite rim (dark gray) surrounds the residual peridotite highlighting the widespread activity of the melt throughout the experiment. (B) Magnified view of the yellow box in (A): Tiny droplets of sulfide are visible along grain boundaries, along which melt has migrated. (C) Clinohumite is interpreted to have formed because of a reaction between olivine (Olv) grains and the percolating melt. The black box shows the location of the TEM lamella, which was extracted for TEM analysis. This location is also highlighted by the white box in (A).

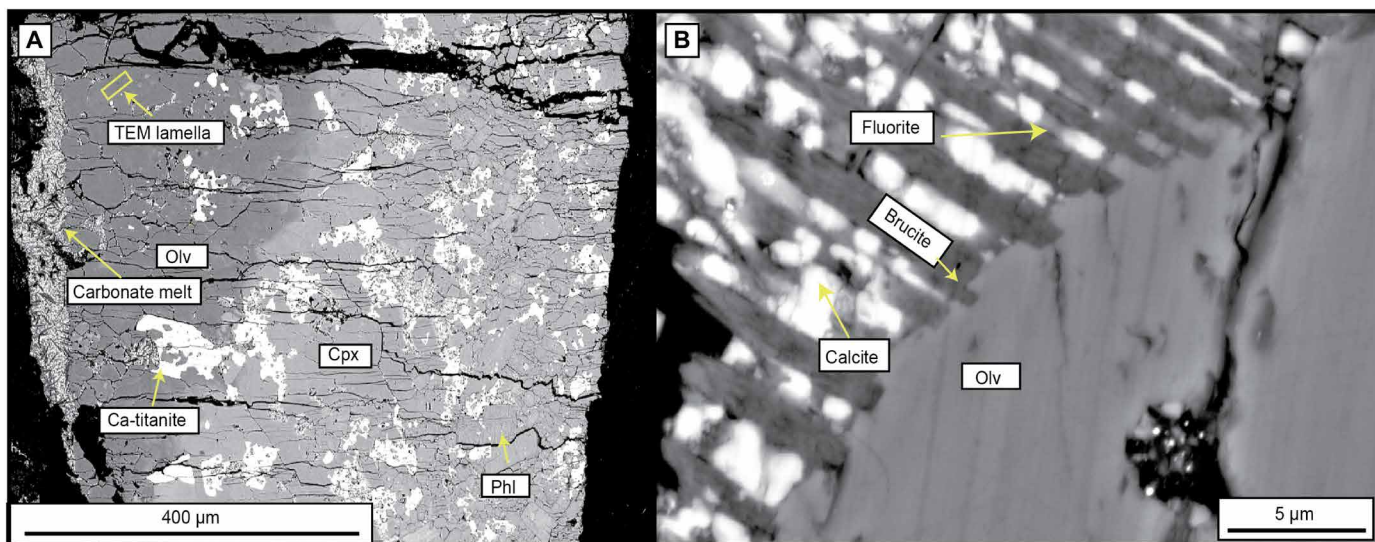


Fig. 2. Back-scattered electron micrographs of M21-107 (2.5GPa, 1050°C—pyroxenite) at different magnifications. (A) Low-magnification overview: Carbonate melts occur along the edges of the experimental charge and are rimmed by olivine (Olv), which has grown as an incongruent melting product as phlogopite began to melt. Clinopyroxene (Cpx), ilmenite (Ilm), and phlogopite (Phl) are present throughout the charge. The yellow box highlights the position of the focused ion beam lamella used for TEM analysis. (B) Magnified view of the carbonate melt quench structure encroaching into the olivine grains. The quenched phases consist of fluorite, brucite, and calcite (identified using TEM-EDS).

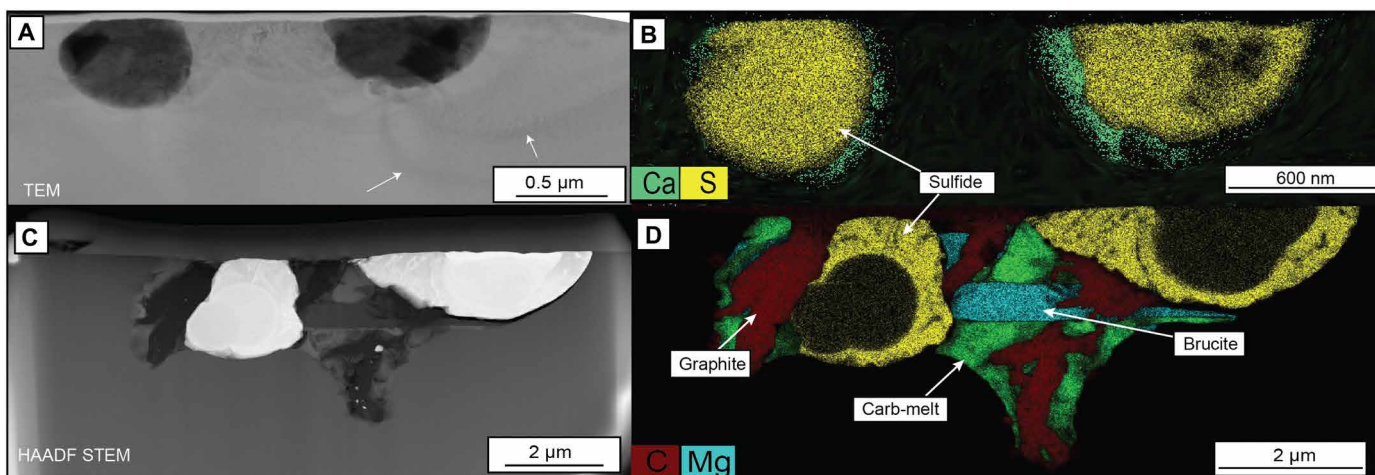


Fig. 3. Transmission electron micrographs and compositional maps of M21-107. (A) TEM image of the peridotite lamella [see Fig. 1 (A and C) for location] showing sulfides in cross-sectional view. The TEM image highlights high-density inclusions within both sulfide blebs. These sulfides occur along an olivine-clinohumite grain boundary and dislocations induced by the growth of the sulfide blebs during quenching are highlighted by the white arrows. A low-density rim surrounds both sulfides and was identified as carbonate melt by TEM-EDS (B). (B) TEM-EDS of the same sulfide blebs: A thin veneer of carbonate melt (green) surrounds both sulfides. (C) High-angle annular dark-field (HAADF) STEM of the pyroxenite lamella (see Fig. 2A). The STEM image shows two sulfide blebs with inner high-density inclusions surrounded by quenched carbonate melt. Graphite is also present in this quenched melt-sulfide complex due to the reduction of carbonate melt to graphite [dark red in (D)]. (D) Four distinct quenched phases were identified with TEM-EDS in the carbonatite that formed during melting of the pyroxenite sample: calcite (CaCO_3), calcium fluoride (CaF_2), brucite [$\text{Mg}(\text{OH})_2$], and graphite (C).

peridotite was located between olivine and clinohumite, neither of which contain significant concentrations of Ca. In addition, TEM-EDS of the clinohumite did not show any appreciable Ca. The thin carbonate melt veneer did not contain any Si and Mg either, with concentrations only increasing toward the olivine and clinohumite phases adjacent to the carbonate melt testifying to this being a separate phase from the silicate mineral network.

Quenched carbonate melt also surrounds sulfide blebs in the pyroxenite sample, where a larger volume of melt was identified around them (Fig. 3, C and D). The crystallized quenched components (5, 20, 21, 34, 35) of the carbonate melt are visible in scanning TEM (STEM) images (Fig. 3C) and TEM-EDS (Fig. 3D). Four distinct quenched phases were identified with TEM-EDS in the carbonatite that formed during melting of the pyroxenite sample: calcite (CaCO_3), calcium

fluoride (CaF₂), brucite [Mg(OH)₂], and graphite (C), as shown in Fig. 3 (C and D).

The tiny sulfide blebs (<1 μm) are common along grain boundaries in both peridotite and pyroxenite experiments where melt-present interfaces are visible in the SEM images (Figs. 1 and 2). There is no evidence to suggest that any sulfide melts were interconnected along grain boundaries, as discrete blebs occur tens of micrometers apart. This regular dispersion of microscale sulfide blebs is commonly attributed to dissolved sulfur in melts, which quench out of experimental melts to form tiny sulfide droplets as seen in Fig. 4 (5, 12, 31). The clinohumite within the peridotite sample displays dislocations close to the sulfide blebs (Fig. 3A), suggesting that space was generated for the sulfide blebs that precipitated out from the carbonate melt. The required space for the incompressible sulfide blebs was accommodated by the silicate

network, inducing strain in the clinohumite crystals (Fig. 3A). Sulfide melts typically require at least 5 vol % of sulfide liquid to interconnect within a four-phase peridotite matrix (36). As it is unlikely that any sulfide liquids would have reached this interconnectivity threshold in the experiments presented here, their presence along grain boundaries implies physical mobilization coupled to the extremely mobile carbonate melts, which are able to interconnect at melt volumes of just 0.3% (37).

Distribution of chalcophile and siderophile elements in carbonate melts

The STEM analysis of the sulfide blebs revealed the presence of high-density cores, which were chemically analyzed using TEM-EDS and found to be inclusions of PGEs. The PGE inclusion within the peridotite-hosted sulfide bleb comprises Pt, Re, Ru, and Ir (Fig. 4),

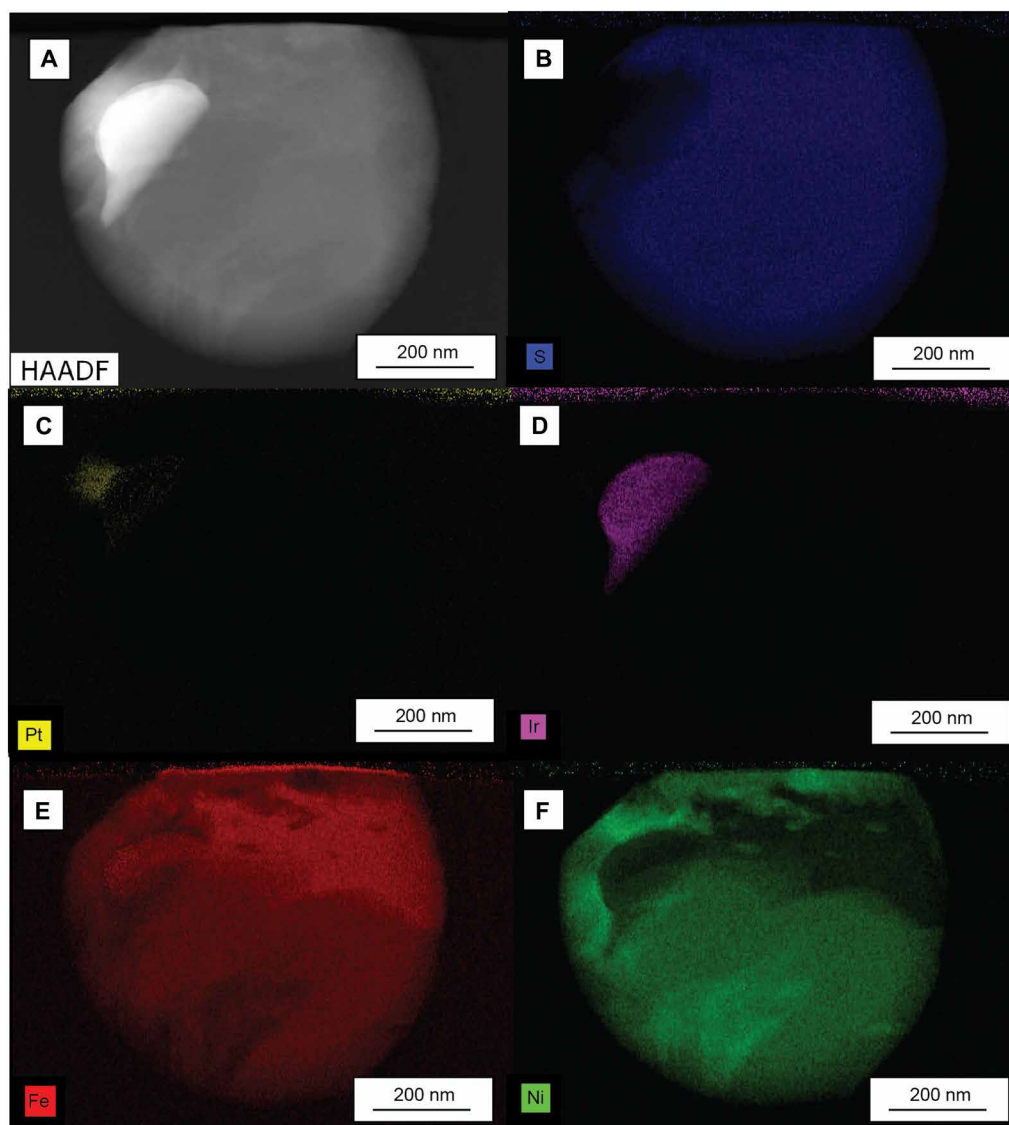


Fig. 4. Transmission electron micrograph and compositional maps of M21-107 peridotite sulfide bleb. (A) HAADF image of the left sulfide bleb from Fig. 3A. The PGE-rich high-density inclusion is visible as the bright white area contained within the sulfide. (B to F) EDS maps of the sulfide bleb showing the distribution of sulfur (B), platinum (C), iridium (D), iron (E), and nickel (F). There is no detectable sulfur within the PGE inclusion (cf. table S7).

while the sulfide bleb in the pyroxenite is rich in Pt and Rh (Fig. 5 and table S7).

PGEs are known to strongly partition into sulfides and refractory metal alloys (6) during melting of silicate mantle rocks. However, the partitioning behavior of PGEs during low-degree melting to produce carbonate melts has not been determined, and neither have $D_{\text{PGE}}^{\text{sulfide/carbonate}}$ coefficients. In situ laser ablation inductively coupled plasma mass spectrometry (LA-ICP-MS) analyses of the pooled carbonate melts segregated at one end of the experimental charge confirmed the presence of elevated PGE concentrations in the carbonate melts, which were also free of sulfide droplets. LA-ICP-MS proved to be advantageous over EDS to circumvent the challenge of interpreting spectral overlaps, allowing easy detection of all PGEs in the ablated melt pockets.

The experiments presented here were not designed to determine $D_{\text{PGE}}^{\text{sulfide/carbonate}}$ coefficients, but our results attest to (i) the mobilization of PGEs in carbonate melts and (ii) the preferential partitioning of PGEs into sulfides in the presence of carbonate melts (Figs. 4 and 5). Similar observations have been experimentally demonstrated in experiments assessing S and PGE solubility in sodic-carbonate systems (38). Texturally, the sulfide blebs appear to have quenched from a liquid, as evidenced by strain and dislocations induced into the surrounding silicate minerals (Fig. 3) and by the variation of the sulfide compositions between the peridotite and pyroxenite assemblages. The sulfides in the peridotite sample are Fe-Ni-sulfide (Fig. 4), while those present in the pyroxenite sample are Fe-Rh-sulfide. The sulfides in both mantle compositions have sequestered some chalcophile elements (Ni, Cu, Co, and Fe) requiring diffusion of these elements from the silicate mineral network to the sulfides. The chalcophile elements Ni, Cu, and Co were not added to the starting materials, and their uptake into sulfides must have been assisted by the carbonate melts that percolated along grain boundaries of silicate minerals, such as olivine, exchanging Mg and Ca cations for Fe, Cu, and Co. Additional LA-ICP-MS measurements on the peridotitic olivine and neighboring clinohumite confirmed the removal of Fe, Cu, and Co from the mantle olivine into the carbonate melts (Fig. 6).

Carbonate melts typically do not remobilize chalcophile elements but are generally associated with metasomatism and localized enrichments in incompatible elements (38). However, elevated PGE contents have recently been reported in carbonatites, which also contain abundant quenched sulfides (39–41). Akizawa *et al.* (39) reported similar microscale features of quenched sulfides associated with carbonate melts, as described here, from Tahitian mantle xenoliths. STEM-EDS was also used in this study to constrain the nanoscale variations within the quenched sulfides, which had partitioned base metals and PGEs.

Sulfur speciation in carbonate melts

We analyzed the segregated carbonate melts using synchrotron sulfur x-ray absorption near-edge structure (XANES) to determine sulfur speciation of the experimental carbonate melts. Multiple S-XANES spot analyses were taken across the quenched carbonate melts (Fig. 7). Following normalization and peak fitting, S-XANES (8, 42) spectra indicated that most sulfur present within the analyzed regions was sulfate ($\frac{S^{6+}}{\sum S} = 0.92$). Experimentally calibrated models for determining fO_2 from sulfate to total sulfur ratios exist only for silicate melts over a restricted pressure, temperature space (8, 10), which cannot be applied simply to carbonate systems. While fO_2 cannot be precisely determined, the high ratio of sulfate to total sulfur implies that the system was oxidized and at an fO_2 approximate to the sulfide-sulfate transition, which is $\sim\Delta FMQ -1$ to $+2$ for silicate melts at 1.5 GPa (10). Similar constraints on carbonates are not yet available, but recent work investigating sulfur concentration at sulfide saturation in carbonated silicate melts at pressures greater than 2.5 GPa have yielded sulfur concentrations of ~ 800 to 3000 ppm (5). Sulfur concentrations within our experimental melts were 600 to 1000 ppm in the peridotite and 800 to 900 ppm in the pyroxenite, suggesting that the carbonate melts generated here had not reached sulfide saturation.

In addition to S-XANES, photo-induced force microscopy (PiFM) maps were acquired at infrared wave numbers known to correspond to the ν_3 stretching vibration of aqueous sulfate anions (SO_4^{2-}) at

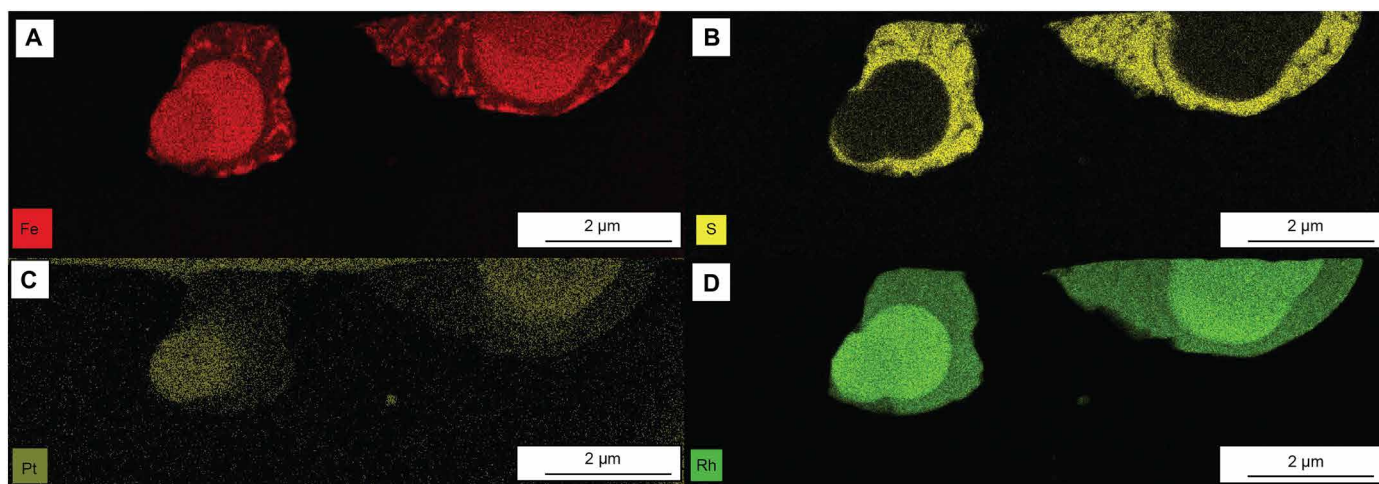


Fig. 5. Transmission electron micrograph compositional maps of M21-107 pyroxenite sulfide bleb. Two distinct Fe-rich PGE inclusions are contained within the sulfide. Compositions of the PGE inclusion within the left sulfide bleb are provided in table S7. EDS maps of (A) iron, (B) sulfur, (C) platinum, and (D) rhodium.

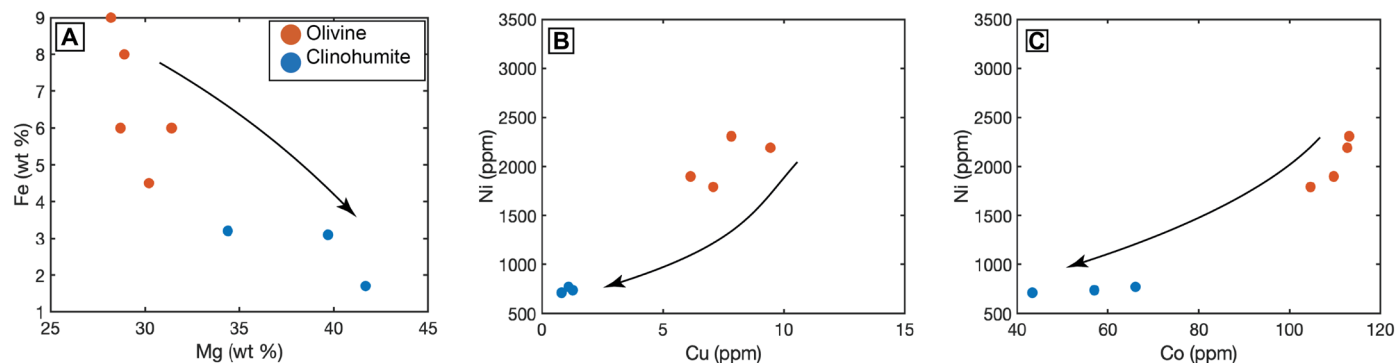


Fig. 6. Chalcophile element compositions of olivine and neighboring clinohumite in M21-107 peridotite. Carbonate melts make their way through silicate rocks by a dissolution and precipitation mechanism, evidenced by the transport of Ni, Cu, Co, and Fe from the silicate minerals to the melt. Typically, carbonate melts do not preferentially include chalcophile elements. However, their strong depletions in clinohumite suggest that sulfate-rich carbonate melts are responsible for this preferential partitioning. The depletion of Fe within the clinohumite is balanced by increased Mg concentrations (A), testifying to the exchange of elements with a percolating melt. The black arrows in (A) to (C) highlight the effect of passing melt on the olivine–clinohumite pairs. (B) The depletion of Ni and Cu in clinohumite relative to olivine. (C) The depletion of Ni and Co in clinohumite relative to olivine.

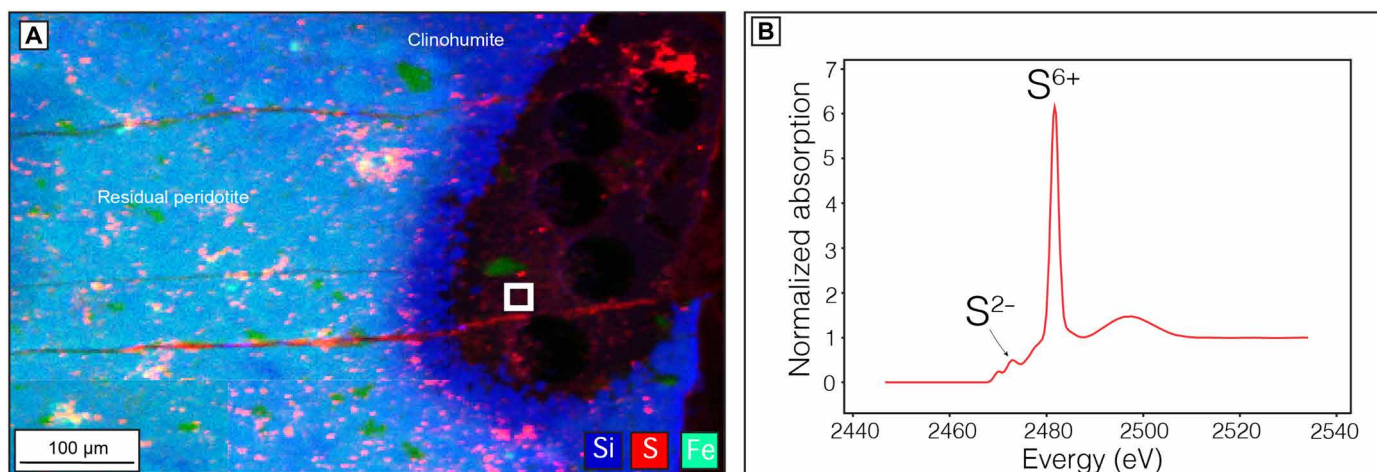


Fig. 7. Synchrotron micro x-ray fluorescence (XRF) map of M21-107 peridotite and accompanying S-XANES. (A) The synchrotron micro-XRF map highlights compositional variations across the sample. Sulfur (red) is concentrated along grain boundaries and within the carbonate melt pool. The clinohumite rim also shows strong depletions in iron. (B) S-XANES spectrum of the carbonate melt, taken from the white square in (A). Most of the sulfur within the carbonate melt is present as oxidized sulfate (S^{6+}).

1100 cm^{-1} (Fig. 8) (43). The PiFM maps highlight multiple nanometer-sized sulfate particles along grain boundaries, which we interpret to occur as anions within the melt as the ν_3 band splits into several spectral features when the sulfate anion is present within a solid-state medium such as a mineral (43). The distortion of sulfate polyhedral by the incorporation of cations (such as Ca^{2+} and Ba^{2+}) also results in the appearance of ν_1 stretching vibrations (1000 cm^{-1}) (42). The lack of splitting or additional peaks suggests that there was no solid-state bonding of cations to the sulfate anions within the melts. Both the S-XANES (Fig. 7B) and PiFM maps (Fig. 8) testify to the presence of sulfur predominately as dissolved sulfate anions in the melt, which would have required oxidized conditions.

DISCUSSION

Mobilization of base and precious metals by carbonate melts

Mantle melting under anhydrous conditions begins at temperatures above the melting point of monosulfide solid solution [MSS at 2.5 GPa,

1200° to 1230°C (44)], which are the main host of sulfur within the upper mantle. Despite MSS being molten at the onset of mantle melting, sulfides remain immobile until they can dissolve into surrounding silicate melts up to the sulfur concentration at sulfide saturation threshold, which is ~ 1200 ppm in basaltic melts at 1.5 GPa (11). Basaltic melts represent less than 15% partial melting of their mantle source (45) and typically do not exhaust the mantle of MSS, restricting the concentration of metals [Cu ~ 60 ppm (46) and Ni ~ 300 ppm (47)] that can be liberated from the mantle to well below that required to generate economically viable Cu-Ni-(PGE)-S ore deposits (48, 49).

However, the mantle is not anhydrous, and volatile components from the surface including H_2O and CO_2 have been effectively recycled back into the mantle throughout the geological evolution of our planet (50) and are known to significantly depress the solidus at low concentrations [950°C at 2.5 GPa (21)] in localized domains of the mantle. This depressed solidus may be close to, or below, the stability limit for solid MSS, with recent work placing the MSS melting point

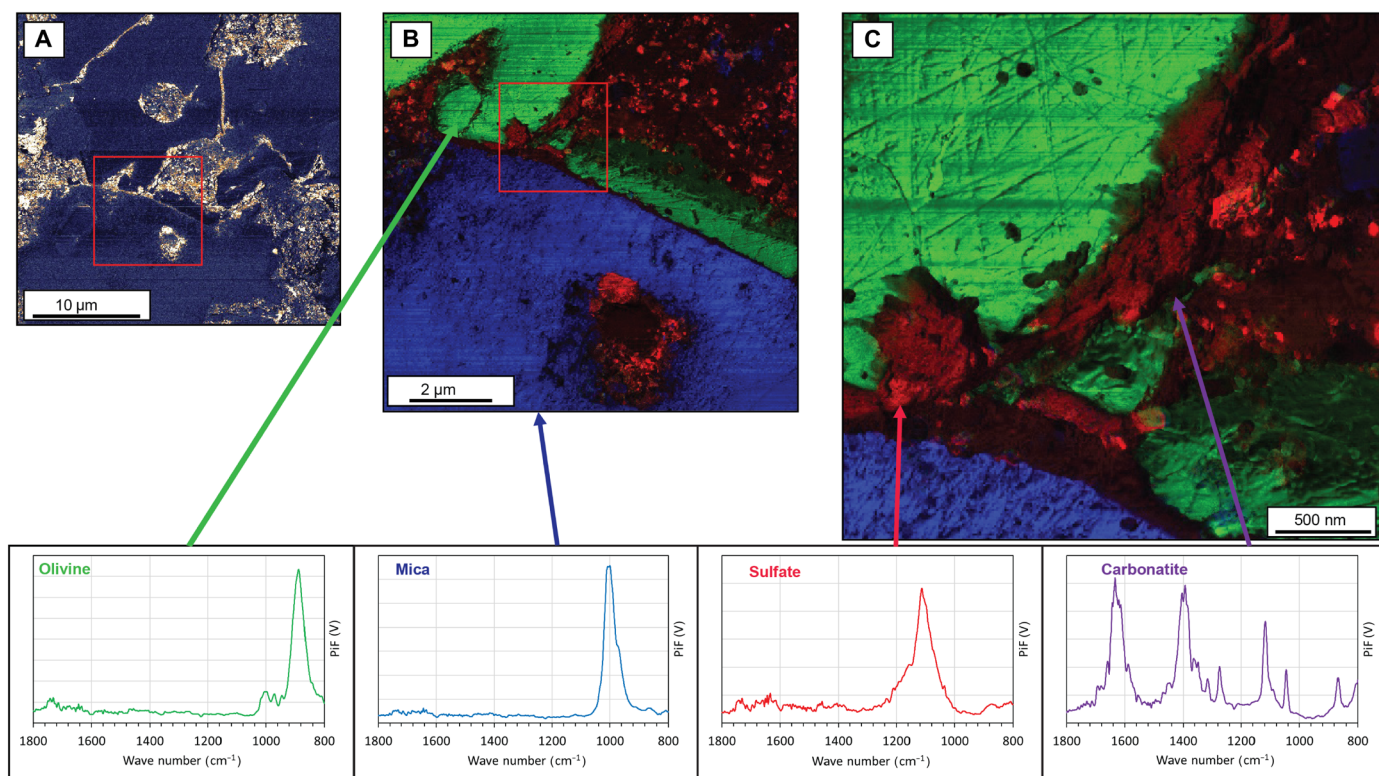


Fig. 8. PiFM map of M21-107 pyroxenite at different magnifications. (A) PiFM map acquired at the sulfate peak (1100 cm^{-1} wave number): The bright gold regions correspond to sulfate, which is predominantly found along grain boundaries between silicate minerals. (B) PiFM map of the red box in (A) combining spectra for olivine (green), mica (blue, phlogopite), and sulfates (red). (C) A high-magnification PiFM map of the red box in (B): Here, interstitial carbonate melt (black) is identified in addition to olivine, mica, and sulfate. The sulfate peaks correspond to aqueous sulfate anions dissolved in the carbonate melt.

at 975° to 1000°C at 2.5 GPa (51). The experiments presented here were run at conditions close to this reported solidus of MSS (51): Therefore, molten sulfide may have been present at the onset of melting. Whether the sulfides were molten or solid at the conditions at which carbonate melts were generated in our experiments is not important, as the ubiquitous presence of sulfate along grain boundaries and in pooled carbonate melts demonstrates that sulfur can be not only dissolved into carbonate melts but also transported away from the residual silicate mantle in moderate concentrations.

Our experiments demonstrate that under sufficiently oxidized conditions, sulfur preferentially dissolves as sulfate in the carbonate melts. The oxidation of sulfide to sulfate is balanced by a sequence of redox reactions beginning with reduction of CO_2 from the melts to graphite (Fig. 3D) by counter oxidation of Fe, which increases the ferric iron content of the system allowing for an increased oxidizing potential to above the sulfide-sulfate transition (49). The migrating carbonate melts are mobile because of their low viscosities and become enriched in S, PGEs, and chalcophile elements (Fig. 6), transporting them rapidly away from the residual mantle source, and potentially concentrating them in localized domains of the overlying continental crust.

Carbonate melts can only exist under oxidized conditions in Earth's mantle, where carbonate redox melting may occur at $\Delta\text{FMQ} \geq +1$ at depths of 3 GPa ($\sim 90\text{ km}$) (27) at the solidus for CO_2 - and H_2O -bearing peridotite (21). At more reduced conditions than $\Delta\text{FMQ} +1$ and/or depths greater than 7 GPa , carbonate-rich melts do not exist

because carbon is stable as graphite or diamond and remains stable until these reduced forms of carbon are oxidized to carbonates (27). The prerequisite of oxidized conditions to generate carbonate melts ensures that there is sufficient CO_2 to counterbalance the production of ferric iron, which promotes S oxidation to sulfate. During melting, sulfate anions become enriched in carbonate melts as demonstrated here (Figs. 7 and 8).

Previous experimental work on the partitioning of chalcophile elements (but not PGEs) between sulfate and silicate melts had demonstrated that chalcophile metals prefer sulfate liquids (52). This partitioning behavior may also be responsible for the uptake of PGEs and other chalcophile elements into the carbonate melts along with sulfate. Carbonate and silicate melts have differing melt structures, which may lead to differences in the partitioning of PGEs and other chalcophile elements. Silicate melts are anionic liquids with Si-(Al)-O tetrahedra, typically requiring cations to charge compensate the system. This crystallographic structure limits the abundance of X^{2+} cations that can be incorporated into the silicate liquid structure, whereas X^{3+} cations are preferentially partitioned into silicate melts (53). Conversely, carbonates are ionic liquids consisting of carbonate CO_3^{2-} molecules, and—unlike silicate melts—they are considered to be structureless (54). This lack of structure results in the inability of carbonates to polymerize, allowing Cu, Fe, Co, and Ni metals to bond with the abundant carbonate ions by donating outer electrons (54). This translates into increased solubility of chalcophile elements into carbonate

compared to silicate melts. However, the behavior of sulfates in carbonates warrants further detailed investigations.

Carbonate melt metasomatism and ore genesis

The carbonate melts generated within our experiments represent low-degree, low-volume melts, which are unlikely to reach the surface of the planet. However, they exist in the mantle over an enormous pressure-temperature range (20–22, 55). Because of their low viscosities, carbonate and carbonate silicate melts are efficient metasomatizing agents (56, 57), which are able to rapidly redistribute and locally concentrate elements such as S, PGEs, and other chalcophile elements (Fig. 6). In view of these unique physico-chemical properties and due to the persistence of carbonate melts to low temperatures, we propose an alternate mechanism by which sulfur, PGEs, and base metals can be (i) mobilized in the mantle through the generation of carbonate melts (58) and (ii) concentrated into metasomatized regions of the mantle, creating fertile domains that may play a first order control on the genesis of mineralized regions (58).

These processes are summarized in Fig. 9: In the deep mantle at depths of <200 km (6.5 GPa), small volumes of carbonate melt are generated when the solidus of carbon- and water-bearing peridotite and pyroxenite is exceeded (~1100°C at 6.5 GPa). These low-volume oxidized carbonate melts are extremely mobile (20, 21, 23, 35) and assist in the oxidation of ferrous Fe to ferric Fe and subsequently mantle sulfides to sulfates, which readily dissolve in the carbonate melts along with PGEs and other chalcophile elements. As the melts migrate to shallower depths, the oxidation processes continue and further S, PGEs, and chalcophile elements are transported from the adjacent wall rocks, until either the sulfur concentration at anhydrite saturation is reached within the carbonate melts—this concentration is currently unconstrained—or the percolating carbonate melts freeze

or are exhausted by reacting with overlying mantle or crustal rocks, resulting in the formation of metasomatized domains.

Since the migrating melts also contain H₂O, the metasomatized products are commonly enriched in hydrous phases, which facilitate subsequent remelting and remobilization owing to the low melting temperatures of hydrous assemblages (22). Evidence for this is seen in mantle xenoliths, where sulfides commonly occur together with hydrous and Ti-oxide minerals (56, 59), and regions where the lithospheric mantle outcrops (60). These primed regions within the mantle will have higher concentrations of S, PGEs, and chalcophile elements relative to surrounding mantle lithologies and will require only a small heat anomaly or lithospheric thinning to remelt before interacting with the crust (61). This final reheating and melting event can potentially lead to supersaturation of S in the resultant alkaline ultramafic melts.

This type of re-enrichment process telescopes metals from an extensive depth range into a more restricted depth window at shallower depths of the mantle. It has been used extensively to argue for the generation of volatile-rich melts such as kimberlites, ultramafic lamprophyres, and lamproites (61, 62). Furthermore, new working hypotheses associated with similar multistage processes of metal mobilization and extraction from metasomatized domains of the mantle have been recently put forward to explain the genesis of Ni-Cu-PGE mineralization hosted in alkaline ultramafic melts emplaced in the lower continental crust (28, 59, 63, 64), and orogenic Au in close proximity to ultramafic lamprophyres in continental settings (65). Their spatial and temporal co-occurrence is consistent with a complex two-stage melting of an oxidized mantle lithology where incipient melts pre-fertilize discrete domains of the source with elevated PGEs and chalcophile elements, which can be subsequently entrained by larger volumes of melts that can accumulate metal-rich sulfides at various

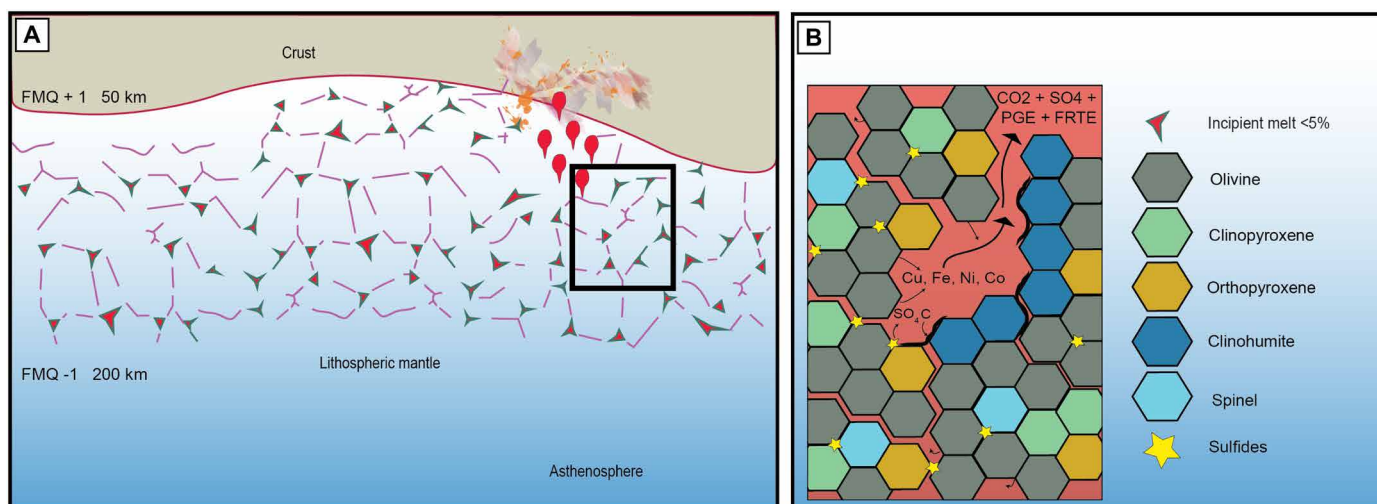


Fig. 9. Schematic diagram of melting processes in the lithospheric mantle. (A) Incipient melts are likely widespread throughout the lithospheric mantle where small amounts of CO₂ and H₂O significantly depress the solidus of peridotite and pyroxenite to temperatures of ~950°C at 2.5 GPa. The first formed melts are carbonatitic in composition, provided oxidized conditions persist. The lithospheric mantle is oxidized enough at depths less than 200 km, and carbon occurs as carbonates in preference to its reduced form of diamond or graphite. (B) The oxidized carbonate melt can interconnect at tiny volumes and, as documented here, transport sulfur as sulfate. This effectively mobilizes sulfur from its mantle reservoir to shallower depths within Earth. The addition of sulfate anions to the melt likely causes a chemical potential gradient and chalcophile elements (Cu, Fe, Ni, and Co) partition strongly from olivine into the sulfate-carbonate melt, along with PGEs. These highly mobile low-degree melts quickly leave their mantle sources and rise toward the crust, where they will react and metasomatize the deep lower crust, enriching it with precious elements that are essential for ore genesis.

crustal levels (28). The Ni-Cu-Co deposit at Voisey's Bay is also closely associated with products of mantle metasomatism, namely, the 1.37-Ga lamproites that precede the 1.34-Ga deposit (66). Evidence for mantle metasomatism is widespread in Newfoundland and Labrador, with lamproites, ultramafic lamprophyres, and carbonatites occurring over an area 100 km north and south of Voisey's Bay (66). This type of extensive multistage infiltration by hydrous-carbonate melts is a common feature of Ni-Fe-Cu-PGE mineralization hosted in the Ivrea zone (67), where the dry and refractory lower crust was fertilized with volatile and incompatible elements through multiple melt injection episodes concentrating the mineralization into ultramafic pipes that acted as melt conduits (67). Another scenario to illustrate this process may have also generated mineralization associated with Siberian picrites (68), which have elevated PGE and Au contents and higher concentrations of sulfur than would be expected if these metals were only present in sulfide in these melts. Mungall *et al.* (68) interpreted the Siberian picrites as having attained their elevated PGE contents by low degrees of partial melting (2.4%) from a mantle source, albeit peridotite, at oxidized conditions (FMQ +2).

This mechanism of sulfur removal from the mantle may operate only locally within previously metasomatized regions of the mantle. However, continued episodic fluxing of low-volume carbonate melts, which are probably more widespread in the mantle than previously thought, would remove the requirement for large degrees of partial melting to exhaust mantle sulfides and generate metal-rich primitive melts. A corollary of this hypothesis is that metallogenically fertile regions of the mantle may be identified in areas that were previously deemed to be nonprospective.

MATERIALS AND METHODS

Two natural mantle xenoliths were chosen as end members for peridotite and pyroxenite starting lithologies. A fresh spinel lherzolite from Lake Nyos was chosen as the representative end member for a peridotite, and the pyroxenite is a mica pyroxenite from Lake Katwe, Uganda. Compositions for both starting materials are provided in table S1. Both compositions were doped with small amounts of volatiles, S (0.8 wt % pyroxenite and 0.5 wt % peridotite), and PGEs (800 ppm pyroxenite and 500 ppm peridotite); CO₂ (3 wt % pyroxenite and 2.5 wt % peridotite) was added as carbonates of siderite (FeCO₃) and magnesite (MgCO₃) to maintain the Mg:Fe ratios present within the natural rocks; H₂O was added as brucite [Mg(OH)₂]; S was added as pyrite (FeS₂); and PGEs were added as nitric acid solutions. PGEs were added in concentrations of 500 to 800 ppm to enable detection at the end of high-pressure experiments.

Typical PGE concentrations within unmelted mantle assemblages are ppb-ppm, which are analytically challenging to detect using established techniques such as LA-ICP-MS. To circumvent this problem, the starting materials were doped to concentrations that could easily be detected and that the relative mobility of PGEs could be traced if they entered the carbonated melts. The concentrations reported at the end of experiments are not used to represent concentrations that would be expected in natural incipient carbonate melts. The rock powders were initially dried at 250°C to liberate adsorbed water before PGEs in solution were added and further dried overnight at 750°C to liberate the nitric acid before finally adding the volatile components and sulfide.

All experiments were conducted in the high-pressure laboratory at Macquarie University using a rapid-quenching end-loaded piston

cylinder apparatus with a ½-inch talc-Pyrex and natural CaF₂ assemblies (32). The powdered starting materials were loaded into dual-chambered graphite capsules (3 mm length), single-wrapped in 25-μm-thick platinum foil, and placed within MgO sleeves. Temperature was monitored with type B Pt₃₀Rh₇₀-Pt₆Rh₉₄ thermocouples, and pressure calibrations were conducted using the quartz-coesite transition (69) and the albite = jadeite + quartz reaction (70). Thermal gradients present within identical CaF₂ assemblies have been tested elsewhere (71, 72) and are equal to or less than 20°C across the length of the capsule, and, therefore no corrections were applied for temperature to those measured by the thermocouple. All experimental charges were brought to the desired pressure first and then heated to the target temperature in 20 min. Experiments were kept at high pressure and high temperature for 24 hours to ensure that equilibrium had been reached, which can be demonstrated by the similar composition of carbonate melts generated here as described elsewhere (20, 21, 35, 73). Subsequently, power was cut to the furnace and the experiments were quenched to room temperature in less than 10 s. Experimental run conditions and results are detailed in table S2.

Upon recovery of the experimental charges, the capsules were embedded directly into epoxy resin before polishing with baby oil or ethanol in a water-free environment to minimize loss of carbonates or quenched melts. Experimental charges were polished to a 0.25-μm finish using diamond and silicate carbide laps.

Analytical details

All samples were initially imaged at Macquarie University using an FEI field-emission SEM operating at 15 kV and a working distance of 10 mm. Following imaging, chemical compositions for the quenched melts and minerals recovered from experiments were determined using quantitative EDS on a Zeiss EVO SEM fitted with an Oxford Instruments large area Quant-EDS detector operating at 20 kV, calibrated to a beam current of 10 μA and a working distance of 12 mm. To ensure accurate compositions, electron microprobe standards were analyzed before each SEM session to ensure that EDS measurements were within 2% of reported compositions. The compositions of melts and minerals recovered from high-pressure experiments are presented in fig. S1 and tables S3 and S4. The quenched products of carbonate melts are extremely heterogeneous and quench into multiple micrometer-size crystals, large areas of melt were analyzed via quantitative-EDS mapping, and compositions were determined from these large, homogenized areas. Multiple maps were averaged to reproduce the homogenized compositions reported here.

Trace-element and PGE compositions of clinohumite, olivine, and carbonates were determined using LA-ICP-MS at Macquarie Geo-Analytical housed at Macquarie University. Trace element analyses were performed using a Teledyne Photon-Machine Excite Excimer (193 nm) Analyte laser ablation system equipped with a HelEx II active 2-volume cell, coupled to an Agilent 8900 ICP-MS system. The ICP-MS was optimized for sensitivity while ablating National Institute of Standard and Technology Standard Reference Material (NIST SRM) 610 in line scan mode. Ablation spot sizes were 50 μm, ablating at 5 Hz with a laser energy of 7 J cm⁻². Detection limits were improved by mixing 5 ml min⁻¹ of molecular hydrogen gas into the laser carrier gas. (74). Data were acquired by taking a background measurement for 120 s, signal for 60 s, and finishing with a 20-s washout time between each analysis. The NIST SRM 610 reference material was used as the primary reference material (Georem preferred values 2022), and U.S. Geological Survey BHVO-2G was also included as a

secondary standard. Unknowns were measured in blocks of six and were bracketed by analyses of standards. An average of two analysis points were collected for each phase per experiment. Data were processed using GLITTER data reduction software (75). SiO₂ and CaO values determined by Quant-EDS were used as internal standard values for silicate mineral and carbonate melt analyses, respectively. Concentrations of PGEs within carbonate melts are presented in table S5.

Carbonate melts exploit grain boundaries to travel rapidly within a solid silicate rock network infiltrating by a dissolution-precipitation mechanism, which allows for effective and efficient exchange of trace and incompatible elements between the mantle reservoir and percolating melt (37). The infiltration of carbonates through the silicate rock and their relationship to chalcophile and siderophile elements was further investigated here on a single high-pressure experiment (M21-107) at a nano- and microscale using TEM, synchrotron S-XANES, and PiFM.

Sulfur speciation of the carbonate melts in experiment M21-107 was determined using synchrotron S-XANES at the Advanced Photon Source on beamline 13-IDE. S-XANES measurements were collected in fluorescence mode using a Si [1 1 1] monochromator crystal. The sample was placed into a He atmosphere to reduce interaction of the photon beam with the surrounding atmosphere. Peak positions were calibrated by measuring gypsum, which provided an S⁶⁺ peak position at 2481.82 eV. Multiple measurements were collected using a 2- μ m beam diameter and a beam intensity of 2.4×10^{10} photons/s. Sulfur K-edge spectra were collected by scanning between the 2447- and 2533-eV energy range; spectra were collected at 1.5-eV steps between 2447 and 2460, at 0.1-eV steps between 2460 and 2486 eV, and at 1.5-eV steps between 2486 and 2533 eV. A dwell time of 2 s per step was used, and three analyses per sample were obtained.

Synchrotron S-XANES causes photo-reduction of S⁶⁺ to S⁴⁺, as has been demonstrated elsewhere (42). The growth of sulfite was observed in some of the analyses collected as part of this analysis cycle, but the sulfite contribution was small and corrected back to S⁶⁺ using the correction method outlined in Lerner *et al.* (42).

All of the S-XANES spectra were normalized and fitted using XAS viewer within the Larch software package (76). The protocol for fitting normalized spectra was based on the approach outlined in Lerner *et al.* (42); six Gaussian peaks and an error step function for background were simultaneously fitted to the entire energy range measured (2447 to 2533 eV), with bounds for peak width, amplitude, and center guided by the determination of Lerner *et al.* (42). Fitted spectra are presented in figs. S2 and S3.

Two electron-transparent foils were prepared by focused ion beam (FIB, Figs. 1 and 2) milling using an FEI Helios Nanolab G3 CX DualBeam FIB/SEM for TEM at the Centre for Microscopy, Characterisation, and Analysis at the University of Western Australia. TEM foils were prepared first by protecting the sample surface with the deposition of amorphous carbon strips that were 12 μ m long, 2 μ m wide, and 1.5 μ m thick. The locations of TEM foils were chosen along grain boundaries where small sulfide blebs could be seen along a melt pathway in back-scattered electron mode. One foil was cut from the peridotite composition and the second was cut from the pyroxenite.

Following the deposition of the protective carbon strip, material on either side was removed by a gallium ion beam operating at 30 kV and a beam current of 21 nA. This resulted in troughs on either side of the strip, which were 30- μ m-deep trenches; the sample was cleaned and thinned with lower ion beam currents (9.3 nA). An

in situ micromanipulator was attached to the sample using a Pt weld, while the remaining edges of the sample were milled away to create a U-shape cut to liberate the sample. The micromanipulator was used to lift out the sample and transfer it to a copper TEM sample holder, and two additional platinum welds were used to secure the thinned sample to the copper grid. The micromanipulator was freed from the sample, and the sample was thinned to ~100 nm at beam currents varying from 2.5 to 0.43 nA; a final cleaning of the surface was conducted at 5 kV and 15 pA.

Bright-field TEM imaging, high-angle annular dark-field STEM (HAADF-STEM) imaging, and element mapping were carried out using an FEI Titan G2 80-200 TEM/STEM with ChemiSTEM Technology operating at 200 kV. In a bright-field image, heavy element features are dark. In the equivalent HAADF-STEM image, heavy element features appear bright. The element maps were obtained by EDS using the Super-X detector on the Titan with a probe size ~1 nm and a probe current of ~0.3 nA. The EDS spectra and elemental maps were processed using the ESPRIT 2 (Bruker Corporation) software. Spectral maps and quantitative EDS spectra of sulfides in the TEM foils are presented in tables S6 and S7.

PiFM was conducted at the Research School of Earth Sciences at the Australian National University, Canberra to investigate the distribution of sulfate within sample M21-107. PiFM is a phase analytical technique that combines the simultaneous acquisition of atomic force microscopy (AFM) and characteristic molecular compound information with a spatial resolution of ~5 nm, i.e., an infrared spectrometer on the nanoscale (77). The acquisition of the absorption features uses infrared (IR) lasers that are both tunable with respect to wave number and pulse repetition rates that illuminate the sample just below the metal-coated AFM tip. The sample's molecules absorb different wavelengths of the laser according to their composition, which is recorded by the sharp cantilever tip as it is being pulled toward the sample by the induced attractive forces. For sample M21-107, the surface was excited by using a mid-IR range "quantum cascade laser" module (QCL, Block Engineering LLC) consisting of four serially connected gap-free QCLs to sweep across the 800 to 1800 cm⁻¹ range. Absorption features have been identified at 940, 1000, 1100, and 1400 cm⁻¹, which correspond to those found in olivine, (phlogopite)-mica, sulfate, and carbonate, respectively (John Wiley & Sons Inc. SpectraBase).

Supplementary Materials

This PDF file includes:

Figs. S1 to S9
Table S1 to S7
References

REFERENCES AND NOTES

1. J. M. Brenan, Re-Os fractionation by sulfide melt-silicate melt partitioning: A new spin. *Chem. Geol.* **248**, 140–165 (2008).
2. J.-P. Lorand, A. Luguet, O. Alard, Platinum-group element systematics and petrogenetic processing of the continental upper mantle: A review. *Lithos* **164-167**, 2–21 (2013).
3. J. E. Mungall, J. M. Brenan, Partitioning of platinum-group elements and Au between sulfide liquid and basalt and the origins of mantle-crust fractionation of the chalcophile elements. *Geochim. Cosmochim. Acta* **125**, 265–289 (2014).
4. P. J. Jugo, An experimental study of the sulfur content in basaltic melts saturated with immiscible sulfide or sulfate liquids at 1300 C and 1.0 GPa. *J. Petrol.* **46**, 783–798 (2004).
5. P. Chowdhury, R. Dasgupta, Sulfur extraction via carbonated melts from sulfide-bearing mantle lithologies—Implications for deep sulfur cycle and mantle redox. *Geochim. Cosmochim. Acta* **269**, 376–397 (2020).

6. M. E. Fleet, W. E. Stone, J. H. Crocket, Partitioning of palladium, iridium, and platinum between sulfide liquid and basalt melt: Effects of melt composition, concentration, and oxygen fugacity. *Geochim. Cosmochim. Acta* **55**, 2545–2554 (1991).
7. A. J. Naldrett, Ultramafic and related mafic rocks; their classification and genesis with special reference to the concentration of nickel sulfides and platinum-group elements. *Econ. Geol.* **71**, 1131–1158 (1976).
8. P. J. Jugo, M. Wilke, R. E. Botcharnikov, Sulfur K-edge XANES analysis of natural and synthetic basaltic glasses: Implications for S speciation and S content as function of oxygen fugacity. *Geochim. Cosmochim. Acta* **74**, 5926–5938 (2010).
9. D. H. Green, T. J. Falloon, Pyrolyte: A ringwood concept and its current expression, in *The Earth's Mantle: Composition, Structure and Evolution*, I. N. S. Jackson, Ed. (Cambridge Univ. Press, 1998), pp. 311–380.
10. V. Matjuschkin, J. D. Blundy, R. A. Brooker, The effect of pressure on sulphur speciation in mid- to deep-crustal arc magmas and implications for the formation of porphyry copper deposits. *Contrib. Mineral. Petrol.* **171**, 66 (2016).
11. P. J. Jugo, Sulfur content at sulfide saturation in oxidized magmas. *Geology* **37**, 415–418 (2009).
12. A. Rielli, A. G. Tomkins, O. Nebel, J. Brugger, B. Etschmann, K. A. Evans, J. L. Wykes, P. Vasilyev, D. J. Paterson, Incipient metal and sulfur extraction during melting of metasomatised mantle. *Earth Planet. Sci. Lett.* **599**, 117850 (2022).
13. M. Locmelis, M. L. Fiorentini, S. J. Barnes, E. J. Hanski, A. F. Kobussen, Ruthenium in chromite as indicator for magmatic sulfide liquid equilibration in mafic-ultramafic systems. *Ore Geol. Rev.* **97**, 152–170 (2018).
14. M. Locmelis, R. D. Arevalo, I. S. Puchtel, M. L. Fiorentini, E. G. Nisbet, Transition metals in komatiitic olivine: Proxies for mantle composition, redox conditions, and sulfide mineralization potential. *Am. Mineral.* **104**, 1143–1155 (2019).
15. P. Sattari, J. M. Brenan, I. Horn, W. F. McDonough, Experimental constraints on the sulfide- and chromite-silicate melt partitioning behavior of rhenium and platinum-group elements. *Econ. Geol.* **97**, 385–398 (2002).
16. G. Iacono-Marziano, M. Le Vaillant, B. M. Godel, S. J. Barnes, L. Arbaret, The critical role of magma degassing in sulphide melt mobility and metal enrichment. *Nat. Comm.* **13**, 2359 (2022).
17. A. Bénard, K. Klimm, A. B. Woodland, R. J. Arculus, M. Wilke, R. E. Botcharnikov, N. Shimizu, O. Nebel, C. Rivard, D. A. Ionov, Oxidising agents in sub-arc mantle melts link slab devolatilisation and arc magmas. *Nat. Comm.* **9**, 3500 (2018).
18. S. Tassara, J. J. Ague, A role for crustal assimilation in the formation of copper-rich reservoirs at the base of continental arcs. *Econ. Geol.* **117**, 1481–1496 (2022).
19. S. Tassara, J. M. Gonzalez-Jiménez, M. Reich, E. Saunders, A. Luguet, D. Morata, M. Grégoire, D. van Acken, M. E. Schilling, F. Barra, G. Nowell, A. Corgne, Highly siderophile elements mobility in the subcontinental lithospheric mantle beneath southern Patagonia. *Lithos* **314–315**, 579–596 (2018).
20. Z. Pintér, S. F. Foley, G. M. Yaxley, A. Rosenthal, R. P. Rapp, A. W. Lanati, T. Rushmer, Experimental investigation of the composition of incipient melts in upper mantle peridotites in the presence of CO₂ and H₂O. *Lithos* **396–397**, 106224 (2021).
21. M. E. Wallace, D. H. Green, An experimental determination of primary carbonatite magma composition. *Nature* **335**, 343–346 (1988).
22. R. Dasgupta, A. Mallik, K. Tsuno, A. C. Withers, G. Hirth, M. M. Hirschmann, Carbon-dioxide-rich silicate melt in the Earth's upper mantle. *Nature* **493**, 211–215 (2013).
23. D. H. Green, Experimental petrology of peridotites, including effects of water and carbon on melting in the Earth's upper mantle. *Phys. Chem. Minerals* **42**, 95–122 (2015).
24. G. M. Yaxley, D. H. Green, V. Kamenetsky, Carbonatite metasomatism in the southeastern Australian lithosphere. *J. Petrol.* **39**, 1917–1930 (1998).
25. S. Aulbach, A.-B. Lin, Y. Weiss, G. M. Yaxley, Wehrlites from continental mantle monitor the passage and degassing of carbonated melts. *Geochem. Persp. Lett.* **30–34**, 30–34 (2020).
26. T. J. Falloon, D. H. Green, Solidus of carbonated fertile peridotite under fluid-saturated conditions. *Geology* **18**, 195–199 (1990).
27. S. F. Foley, Redox Melting in the mantle, in *Geophysical Monograph Series*, R. Moretti, D. R. Neuville Eds. (Wiley, 2021), pp. 93–113.
28. S. Ghosh, E. Ohtani, K. D. Litavos, H. Terasaki, Solidus of carbonated peridotite from 10 to 20 GPa and origin of magnesiocarbonatite melt in the Earth's deep mantle. *Chem. Geol.* **262**, 17–28 (2009).
29. D. E. Blanks, D. A. Holwell, M. L. Fiorentini, M. Moroni, A. Giuliani, S. Tassara, J. M. Gonzalez-Jimenez, A. J. Boyce, E. Ferrari, Fluxing of mantle carbon as a physical agent for metallogenetic fertilization of the crust. *Nat. Comm.* **11**, 4342 (2020).
30. H. S. R. Hughes, I. McDonald, M. Looke, I. B. Butler, B. G. K. Upton, J. W. Faithfull, Paradoxical co-existing base metal sulphides in the mantle: The multi-event record preserved in Loch Roag peridotite xenoliths, North Atlantic craton. *Lithos* **276**, 103–121 (2017).
31. A. B. Woodland, A. V. Girsin, V. K. Bulatov, G. P. Brey, H. E. Höfer, Experimental study of sulfur solubility in silicate-carbonate melts at 5–10.5 GPa. *Chem. Geol.* **505**, 12–22 (2019).
32. L. Jia, Y. Chen, B. Su, Q. Mao, D. Zhang, Oxygen-fugacity evolution of magmatic Ni-Cu sulfide deposits in East Kunlun: Insights from Cr-spinel composition. *Am. Mineral.* **107**, 1968–1981 (2022).
33. I. S. Ezad, S. S. Shcheka, S. Buhre, A. Buhre, L. R. Gorojovsky, J. J. Shea, M. W. Förster, S. F. Foley, Rapid quench piston cylinder apparatus: An improved design for the recovery of volatile-rich geological glasses from experiments at 0.5–2.5 GPa. *Rev. Sci. Instrum.* **94**, 055107 (2023).
34. R. Dasgupta, M. M. Hirschmann, Melting in the Earth's deep upper mantle caused by carbon dioxide. *Nature* **440**, 659–662 (2006).
35. S. F. Foley, G. M. Yaxley, A. Roenthal, S. Buhre, E. S. Kiseeva, R. P. Rapp, D. E. Jacob, The composition of near-solidus melts of peridotite in the presence of CO₂ and H₂O between 40 and 60 kbar. *Lithos* **112**, 274–283 (2009).
36. T. Yoshino, M. J. Walter, T. Katsura, Connectivity of molten Fe alloy in peridotite based on in situ electrical conductivity measurements: Implications for core formation in terrestrial planets. *Earth Planet. Sci. Lett.* **222**, 625–643 (2004).
37. T. Hammouda, D. Laporte, Ultrafast mantle impregnation by carbonatite melts. *Geology* **28**, 283–285 (2000).
38. C. Jorgenson, "Sulphur solubility of carbonatites as a mass transfer agent in the mantle," thesis, Dalhousie University (2017).
39. N. Akizawa, A. Miyake, A. Ishikawa, A. Tamura, Y. Terada, K. Uesugi, A. Takeuchi, S. Arai, C. Tanaka, Y. Igami, K. Suzuki, T. Kogiso, Metasomatic PGE mobilization by carbonatitic melt in the mantle: Evidence from sub- μm -scale sulfide-carbonaceous glass inclusion in Tahitian harzburgite xenolith. *Chem. Geol.* **475**, 87–104 (2017).
40. L. Ackerman, L. Polak, T. Mgna, V. Rappich, J. Durisova, D. Upadhyay, Highly siderophile element geochemistry and Re–Os isotopic systematics of carbonatites: Insights from Tamil Nadu, India. *Earth Planet. Sci. Lett.* **520**, 175–187 (2019).
41. D. He, Y. Liu, F. Moynier, S. F. Foley, C. Chen, Platinum group element mobilization in the mantle enhanced by recycled sedimentary carbonate. *Earth Planet. Sci. Lett.* **541**, 116262 (2020).
42. A. H. Lerner, M. J. Muth, P. J. Wallace, A. Lanzirotti, M. Newville, G. A. Getani, P. Chowdhury, R. Dasgupta, Improving the reliability of Fe- and S-XANES measurements in silicate glasses: Correcting beam damage and identifying Fe-oxide nanolites in hydrous and anhydrous melt inclusions. *Chem. Geol.* **586**, 120610 (2021).
43. M. D. Lane, Mid-infrared emission spectroscopy of sulfate and sulfate-bearing minerals. *Am. Mineral.* **92**, 1–18 (2007).
44. Z. Zhang, M. M. Hirschmann, Experimental constraints on mantle sulfide melting up to 8 GPa. *Am. Mineral.* **101**, 181–192 (2016).
45. T. J. Falloon, L. V. Danyushevsky, D. H. Green, Peridotite melting at 1 GPa: Reversal experiments on partial melt compositions produced by peridotite-basalt sandwich experiments. *J. Petrol.* **42**, 2363–2390 (2001).
46. C.-T. A. Lee, P. Luffi, E. J. Chin, R. Bouchet, R. Dasgupta, D. M. Morton, V. Le Roux, Q. Z. Yin, D. Jin, Copper systematics in arc magmas and implications for crust-mantle differentiation. *Science* **336**, 64–68 (2012).
47. Z. Yao, K. Qin, J. E. Mungall, Tectonic controls on Ni and Cu contents of primary mantle-derived magmas for the formation of magmatic sulfide deposits. *Am. Mineral.* **103**, 1545–1567 (2018).
48. A. J. Naldrett, Secular variation of magmatic sulfide deposits and their source magmas. *Econ. Geol.* **105**, 669–688 (2010).
49. J. E. Mungall, Roasting the mantle: Slab melting and the genesis of major Au and Au-rich Cu deposits. *Geology* **30**, 915–918 (2002).
50. E. Cannò, M. Tiepolo, G. E. Bebout, M. Scambelluri, Into the deep and beyond: Carbon and nitrogen subduction recycling in secondary peridotites. *Earth Planet. Sci. Lett.* **543**, 116328 (2020).
51. C. Beyer, T. Bissbort, R. Hartmann, J. Berndt, S. Klemme, R. O. C. Fonseca, High-pressure phase relations in the system Fe–Ni–Cu–S up to 14 GPa: Implications for the stability of sulfides in the Earth's upper mantle. *Contrib. Mineral. Petrol.* **177**, 99 (2022).
52. I. V. Veksler, A. M. Dorfmann, P. Dulski, V. S. Kamenetsky, L. V. Danyushevsky, T. Jeffries, D. B. Dingwell, Partitioning of elements between silicate melt and immiscible fluoride, chloride, carbonate, phosphate and sulfate melts, with implications to the origin of natrocarbonatite. *Geochim. Cosmochim. Acta* **79**, 20–40 (2012).
53. B. O. Mysen, The structure of silicate melts. *Annu. Rev. Earth Planet. Sci.* **11**, 75–97 (1983).
54. A. P. Jones, M. Genge, L. Carmody, Carbonate melts and carbonatites. *Rev. Mineral. Geochem.* **75**, 289–322 (2013).
55. R. Dasgupta, M. M. Hirschmann, The deep carbon cycle and melting in Earth's interior. *Earth Planet. Sci. Lett.* **298**, 1–13 (2010).
56. J. E. Saunders, N. J. Pearson, S. Y. O'Reilly, W. L. Griffin, Sulfide metasomatism and the mobility of gold in the lithospheric mantle. *Chem. Geol.* **410**, 149–161 (2015).
57. W. Powell, S. O'Reilly, Metasomatism and sulfide mobility in lithospheric mantle beneath eastern Australia: Implications for mantle Re–Os chronology. *Lithos* **94**, 132–147 (2007).
58. C. Xu, L. Qi, Z. Huang, Y. Chen, X. Yu, L. Wang, E. Li, Abundances and significance of platinum group elements in carbonatites from China. *Lithos* **105**, 201–207 (2008).
59. B. Harte, P. A. Winterburn, J. J. Gurney, Metasomatic and enrichment phenomena in garnet peridotite facies mantle xenoliths from the Matsoku kimberlite pipe, Lesotho, in *Mantle Metasomatism*, M. A. Menzies, C. J. Hawkesworth, Eds. (Academic Press, 1987), pp. 145–220.

60. M. L. Fiorentini, C. LaFlamme, S. Denyszyn, D. Mole, R. Maas, M. Locmelis, S. Caruso, T. H. Bui, Post-collisional alkaline magmatism as gateway for metal and sulfur enrichment of the continental lower crust. *Geochim. Cosmochim. Acta* **223**, 175–197 (2018).
61. S. F. Foley, T. P. Fischer, An essential role for continental rifts and lithosphere in the deep carbon cycle. *Nat. Geosci.* **10**, 897–902 (2017).
62. I. S. Ezad, S. F. Foley, Experimental partitioning of fluorine and barium in lamproites. *Am. Mineral.* **107**, 2008–2019 (2022).
63. S. F. Foley, I. S. Ezad, S. R. van der Laan, M. Pertermann, Melting of hydrous pyroxenites with alkali amphiboles in the continental mantle: 1. Melting relations and major element compositions of melts. *Geosci. Front.* **13**, 101380 (2022).
64. M. Locmelis, M. L. Fiorentini, T. Rushmer, R. Arevalo, J. Adam, S. W. Denyszyn, Sulfur and metal fertilization of the lower continental crust. *Lithos* **244**, 74–93 (2016).
65. Y. Lu, C. M. Lesher, J. Deng, Geochemistry and genesis of magmatic Ni-Cu-(PGE) and PGE-(Cu)-(Ni) deposits in China. *Ore Geol. Rev.* **107**, 863–887 (2019).
66. S. Tappe, S. F. Foley, G. A. Jenner, L. M. Heaman, B. A. Kjargaard, R. L. Romer, A. Stracje, N. Joyce, J. Hoefs, Genesis of ultramafic lamprophyres and carbonatites at Aillik Bay, Labrador: A consequence of incipient lithospheric thinning beneath the North Atlantic Craton. *J. Petrol.* **47**, 1261–1315 (2006).
67. G. Sessa, M. Moroni, S. Tumiatì, S. Caruso, M. L. Fiorentini, Ni-Fe-Cu-PGE ore deposition driven by metasomatic fluids and melt-rock reactions in the deep crust: The ultramafic pipe of Valmaggia, Ivrea-Verbano, Italy. *Ore Geol. Rev.* **90**, 485–509 (2017).
68. J. E. Mungall, J. J. Hanley, N. T. Arndt, A. Debecdelievre, Evidence from meimechites and other low-degree mantle melts for redox controls on mantle-crust fractionation of platinum-group elements. *Proc. Nat. Acad. Sci. U.S.A.* **103**, 12695–12700 (2006).
69. J. P. Perrillat, I. Daniel, J. M. Lardeaux, H. Cardon, Kinetics of the coesite-quartz transition: Application to the exhumation of ultrahigh-pressure rocks. *J. Petrol.* **44**, 773–788 (2003).
70. T. J. B. Holland, The reaction albite=jadeite+ quartz determined experimentally in the range 600–1200 degrees C. *Am. Mineral.* **65**, 129–134 (1980).
71. F. Schilling, B. Wunder, Temperature distribution in piston-cylinder assemblies: Numerical simulations and laboratory experiments. *Eur. J. Mineral.* **16**, 7–14 (2004).
72. N. Farmer, “Archives of experimental conditions in solid media apparatus: A new method of determining pressure and temperature applied to a re-evaluation of piston-cylinder techniques and the spinel to garnet phase transition,” thesis, The Australian National University (2021).
73. R. J. Sweeney, Carbonatite melt compositions in the Earth’s mantle. *Earth Planet. Sci. Lett.* **128**, 259–270 (1994).
74. L. Gorjovsky, O. Alard, Optimisation of laser and mass spectrometer parameters for their situ analysis of Rb/Sr ratios by LA-ICP-MS/MS. *J. Anal. Atom. Spectr.* **35**, 2322–2336 (2020).
75. W. L. Griffin, W. J. Powell, N. J. O. Pearson, S. Y. Reilly, GLITTER: Data reduction software for laser ablation ICP-MS. *Laser Ablation ICP-MS Earth Sci.* **40**, 204–207 (2008).
76. M. Newville, Larch: An analysis package for XAFS and related spectroscopies. *J. Phys. Conf. Ser.* **430**, 012007 (2013).
77. L. M. Otter, M. W. Förster, E. Belousova, P. O’Reilly, D. Nowak, S. Park, S. Clark, S. F. Foley, D. E. Jacob, Nanoscale chemical imaging by photo-induced force microscopy: Technical aspects and application to the geosciences. *Geostand. Geoanal. Res.* **45**, 5–27 (2021).
78. O. Von Knorring, C. Du Bois, Carbonatitic lava from fort portal area in Western Uganda. *Nature* **192**, 1064–1065 (1961).
79. J. Gittins, R. H. Hewins, Kimberlitic-carbonatitic dikes of the Saguenay River Valley, Quebec, Canada. *Canada. Phys. Chem. Earth* **9**, 137–148 (1975).
80. J. B. Dawson, M. S. Garson, B. Roberts, Altered former alkalic carbonatite lava from Oldoinyo Lengai, Tanzania: Inferences for calcite carbonatite lavas. *Geology* **15**, 765 (1987).
81. T. Guzmics, Z. Zajacz, R. H. Mitchell, C. Szabó, M. Wälle, The role of liquid–liquid immiscibility and crystal fractionation in the genesis of carbonatite magmas: Insights from Kerimasi melt inclusions. *Contrib. Mineral. Petrol.* **169**, 17 (2015).
82. D. Weidendorfer, M. W. Schmidt, H. B. Mattsson, A common origin of carbonatite magmas. *Geology* **45**, 507–510 (2017).

Acknowledgments: We thank S. Murray for assistance with high-resolution SEM images at Macquarie University and E. Sirantoine for cutting both FIB lamellae and preparing the TEM samples. We also thank M. Newville, A. Lanzirotti, and S. Hunt for support and assistance during beamtime operations at GSECARS 13-IDE. Synchrotron XRF mapping and S-XANES data were collected during beam time awarded to I.S.E. Portions of this work were performed at GeoSoilEnviroCARS (The University of Chicago, Sector 13-IDE), Advanced Photon Source (APS), and Argonne National Laboratory. GeoSoilEnviroCARS is supported by the National Science Foundation–Earth Sciences (EAR-1634415). **Funding:** This work was funded by the ARC Laureate Fellowship FL180100134 awarded to S.F.F. This research used resources of the Advanced Photon Source, a U.S. Department of Energy (DOE) Office of Science User Facility operated for the DOR Office of Science by Argonne National Laboratory under contract no. DE-AC02-06CH11357. We acknowledge the facilities and the scientific and technical assistance of Microscopy Australia and the Centre for Microscopy, Characterisation, and Analysis, The University of Western Australia, a facility funded by the University, State, and Commonwealth Governments of Australia. **Author contributions:** Conceptualization: I.S.E., S.F.F., M.L.F., and M.W.F. Methodology: I.S.E., S.F.F., S.S.S., M.S., L.R.G., and M.W.F. Investigation: I.S.E., S.F.F., M.L.F., S.S.S., L.R.G., M.W.F., and M.S. Visualization: I.S.E., S.F.F., M.L.F., M.S., and M.W.F. Supervision: S.F.F. and M.L.F. Writing—original draft: I.S.E., S.F.F., L.R.G., and M.S. Writing—review and editing: I.S.E., S.F.F., M.L.F., L.R.G., S.S.S., and M.W.F. Formal analysis: I.S.E. and M.S. Validation: S.S.S., M.W.F., and I.S.E. Resources: S.S.S., L.R.G., and S.F.F. Funding acquisition: S.F.F. and M.L.F. **Competing interests:** The authors declare that they have no competing interests. **Data and materials availability:** All data needed to evaluate the conclusions in the paper are present in the paper and/or the Supplementary Materials.

Submitted 30 August 2023

Accepted 20 February 2024

Published 22 March 2024

10.1126/sciadv.adk5979